Force, diffusion, and channeling in sub-Doppler laser cooling

M. D. Hoogerland,* H. F. P. de Bie, H. C. W. Beijerinck, E. J. D. Vredenbregt, and K. A. H. van Leeuwen
Physics Department, Eindhoven University of Technology, P.O. Box 513, 5600 MB Eindhoven, The Netherlands

P. van der Straten
Debye Institute, Vakgroep Atoom- en Grenslaagfysika, Utrecht University, P.O. Box 80000, 3508TA Utrecht, The Netherlands

H. J. Metcalf
State University of New York at Stony Brook, Stony Brook, New York 11794
(Received 3 October 1995; revised manuscript received 3 April 1996)

We present an extensive set of measurements on one-dimensional sub-Doppler cooling and channeling in counterpropagating light beams. The experimental method consists of the measurement of the profile of an initially subrecoil collimated atomic beam, which is deflected by the interaction with the light field. The initial velocity of the atoms in the direction of the laser beams is varied in the range $-1 \leqslant v_{\perp}(\mathrm{ms}^{-1}) \leqslant 1$ by changing the angle between atomic and laser beams. For the orthogonal circular polarization ($\sigma^{+}\sigma^{-}$) sub-Doppler cooling configuration, the force and the diffusion coefficient characterizing the cooling process have been determined as a function of the initial velocity $v_{\perp}$ from the average deflection and broadening of the atomic beam profile. We observe transient effects due to the slow evolution of the distribution over the magnetic sublevels to an equilibrium. The experimental results agree very well with quantum Monte Carlo simulations and semiclassical calculations. For the orthogonal linear polarization ($\pi^{x}\pi^{y}$) configuration, we demonstrate the validity of the well-known Sisyphus picture for the cooling mechanism by comparing the experimental data to the results of a simple semiclassical Monte Carlo model incorporating only the dipole force and optical pumping. In weak standing waves of either circular or linear polarization, we demonstrate the characteristic features of channeling. [S1050-2947(96)07209-5]

PACS number(s): 32.80.Pj, 42.50.Vk

I. INTRODUCTION

Sub-Doppler laser cooling has been studied extensively, both theoretically and experimentally. After the first experiments that demonstrated cooling to temperatures below the Doppler limit [1,2], the relevant physical mechanisms have been identified (leading to the designation ''polarization-gradient laser cooling'') and theoretical descriptions have been developed [3–5]. Experiments have studied the final temperature and velocity distribution [1,6,7] as well as the time dependence of the cooling process [6]. New mechanisms have been discovered and studied [6,8–16]. The references given above are far from complete and do not include schemes leading to even lower temperatures (below the recoil limit), cooling in the presence of restoring forces, or cooling in two or three dimensions. For a more comprehensive list, we refer the reader to recent review articles on laser cooling [17,18].

All experiments on sub-Doppler recoil-limited cooling mentioned above have one thing in common: they start with a relatively broad velocity distribution, which evolves into a narrower distribution during the cooling process. Although the experiments satisfied the theoretical descriptions, the experimental information is by far not as complete as one would want. Semiclassical theoretical approaches, where the evolution of the velocity distribution is described in terms of a Fokker-Planck equation, are characterized by a velocity dependent force $F(v)$ and diffusion coefficient $D(v)$. The idea of a velocity dependent force is, of course, generally basic to the understanding of laser cooling. However, when starting an experiment with a broad velocity distribution, $F(v)$ is impossible to measure. If the only thing that is measured in the experiment is the final velocity distribution after a fixed interaction time, no independent information on the force and diffusion is obtained. If the final distribution can be characterized by a single temperature (i.e., if it is Gaussian), this temperature is fully determined by the ratio of the damping coefficient $(dF/dv)_{v=0}$ to the diffusion coefficient $D(v=0)$ (provided that the width of the final velocity distribution is much smaller than the capture range).

Information on the force $F(v)$ and diffusion coefficient $D(v)$ at $v \neq 0$ is contained in the observed deviation of the final velocity distribution from a Gaussian profile. When the time dependence of the cooling process is studied [4,6] as well, independent information on the force and damping coefficient as a function of velocity can in principle be obtained. However, in practice it is impossible to reconstruct $F(v)$ and $D(v)$ from the results of experiments with a broad initial velocity distribution.

In an earlier article [19] we reported results from experiments on one-dimensional laser cooling with counterpropagating, orthogonal circularly polarized laser beams ($\sigma^{+}\sigma^{-}$ cooling) using a narrow initial velocity distribution (below one photon recoil) and a short interaction time (below the

*Present address: Atomic and Molecular Physics Laboratories, Research School for Physical Sciences and Engineering, Australian National University, Canberra Australia Capital Territory 0200, Australia.

damping time of the cooling process). In these experiments, the deflection of a well-collimated atomic beam intersecting the laser beams (almost) perpendicularly is studied. This can be seen as a true one-dimensional experiment: the velocity in the direction of the k vectors of the laser beams, which is less than 1 ms^{-1}, is strongly influenced by the interaction with the laser light. The axial velocity of the atomic beam, which is on the order of 1200 ms^{-1}, is hardly influenced. The Gaussian laser beam profile in this direction can thus be treated as a variation of the laser intensity in time. The initial velocity in the direction of the laser beam can be varied by moving the slits used to collimate the atomic beam. The width (rms spread) of the velocity distribution in this direction is much smaller than a single photon recoil.

The velocity distribution is modified by the interaction with the laser field: it will be shifted because of an average force on the atoms and broadened, for instance by spontaneous emission heating. If the force exerted on the atoms by the laser field does not depend on the position of the atoms in the light field, as in the $\sigma^+\sigma^-$ configuration, the average velocity change Δv of the atoms can be directly translated to a time-averaged force by defining an effective interaction time with the Gaussian laser beam (see Sec. III C). The broadening of the velocity distribution of the atomic beam can then be translated to a diffusion coefficient, also averaged over the interaction time. Repeating the experiment for a range of initial values of the transverse velocity allows the measurement of the averaged force and diffusion curves $F(v)$ and $D(v)$.

In Ref. [19] we presented the results of such measurements. The resulting force and diffusion curves were compared with semiclassical and fully quantized calculations and showed excellent agreement. It should be stressed that the measured curves do not represent the steady-state force (named ''drag force'' in Ref. [4]) and diffusion coefficient, but are averaged over the interaction time. Marked differences between steady-state and measured values are observed, which are caused by the transient behavior, as predicted by Ungar *et al.* [4].

In this paper we present a more extensive discussion of the measured and calculated data on $\sigma^+\sigma^-$ cooling. Furthermore, the results of experiments using other polarization configurations of the laser beams are presented. The configurations that have been studied are orthogonal linear polarization ($\pi^x\pi^y$, also called lin-perp-lin or sub-Doppler Sisyphus cooling) as well as circular ($\sigma^+\sigma^+$) and linear ($\pi^x\pi^x$) standing waves.

For pure standing waves and in the absence of static fields, no sub-Doppler cooling occurs. Doppler cooling does play a role; however, on the transverse velocity scale of the experiment (<1 m/s) the force is only weakly velocity-dependent. In the standing wave, the atoms experience a periodic dipole potential leading to a strongly position-dependent force. With a relatively long interaction time, this can lead to channeling of the atoms in the ''valleys'' of the dipole potential [20,21]. In our experiment, the position-dependent force causes a broadening and shift of the transverse velocity distribution of the atomic beam which are not connected with a velocity-dependent force and diffusion. Varying the initial transverse velocity of the atoms, we expect a drastic change in the behavior at the classical escape velocity of the atoms from the potential valleys.

For the $\pi^x\pi^y$ configuration, sub-Doppler cooling and channeling are both present, further complicating the analysis of the observed deflection patterns. The sub-Doppler cooling mechanism in this case is called the Sisyphus mechanism. This mechanism can be easily understood in terms of a semiclassical model with the atoms moving in one dipole potential pattern until their internal state changes due to spontaneous emission and they are suddenly transferred to a different potential. Thus, we expect such a simple semiclassical rate-equation model to reproduce the experimental results on the $\pi^x\pi^y$ configuration.

In all cases the deflected beam profiles for different initial transverse velocities provide a thorough check on the channeling phenomenon and the mechanism of the cooling process. Thus, we have measured deflected beam profiles for four polarization configurations as a function of the initial velocity at several values of the laser detuning Δ and laser intensity I. We provide a much more stringent check of the theory than earlier measurements, which used a broad initial velocity distribution. We compare our measured results with existing theories on laser cooling, and find in most cases excellent agreement. Transient effects and channeling in potential wells during the cooling process are observed.

II. THEORY

We compare our measured deflected beam profiles with several theoretical models. First we consider a simple physical picture of the interaction of the atoms with the laser light and implement this in a semiclassical rate-equation-based Monte Carlo simulation of the experiment. Channeling of atoms in a pure standing wave as well as the $\pi^x\pi^y$ cooling configuration are shown to be well understood using this simple model. Second, we use the semiclassical operator treatment of sub-Doppler cooling forces as given by Nienhuis *et al.* [5]. The steady-state drag forces as well as transient effects can be calculated for an arbitrary (one-dimensional) light field using this model. These calculations show fair agreement with the experimental data for all experimental laser configurations. Finally, we consider a fully quantum mechanical Monte Carlo simulation, as introduced by Dum *et al.* [22]. These calculations show excellent agreement with the experimental data for all laser configurations.

A. Semiclassical rate-equation model

A two-level atom with transition frequency ω_0 (wavelength $\lambda_0=2\pi c/\omega_0$) and natural linewidth Γ (upper level lifetime $\tau=1/\Gamma$) in a laser field of angular frequency ω_L and light intensity I experiences a population-averaged ''light shift'' or ac Stark shift equal to

$$\hbar\Omega_s=\frac{\hbar\Delta}{2}\ln\left(1+\frac{\Omega^2}{2\Delta^2}\right). \tag{1}$$

Here, $\Delta=\omega_L-\omega_0$ denotes the detuning of the laser field and Ω the Rabi frequency ($\Omega=[3\lambda_0^3 I/2\pi hc\tau]^{1/2}$). In a pure standing wave of either linear or circular polarization, this means that the atom experiences a spatially modulated potential with maximum absolute values at the antinodes of the standing wave. If the kinetic energy of the atoms is smaller

than the light shift in the antinodes, the atoms will be channeled in the standing wave pattern. The classical particle trajectories in such a periodic potential can easily be calculated, and the resulting deflected beam profiles show a strikingly good agreement with the experimental data. In a numerical simulation of our experiment, we introduced magnetic substates and included optical pumping between these substates as well as momentum diffusion by spontaneous emission in a Monte Carlo procedure. Coherences between the magnetic substates are not taken into account in this approach. We start out with an atom in a particular magnetic substate, and calculate the classical particle trajectory in the potential pattern. Photons are spontaneously emitted at a rate Γn_e, with Γ the natural linewidth of the transition and n_e the excited state fraction. Spontaneous decay may go to another magnetic substate, chosen with the correct probabilities given by the Clebsch-Gordan coefficients.

For the $\pi^x\pi^y$ cooling configuration, the well known physical Sisyphus picture is applicable [3]. In this configuration, the polarization of the resulting light field is spatially modulated, varying from linear polarization to circular to orthogonal linear to orthogonal circular and so on. A moving atom thus experiences a constantly changing polarization of the light field. In a $J\rightarrow J+1$ transition, optical pumping in the light field will tend to drive the atom to the most light shifted magnetic sublevel of the ground state. In case of red detuning, this is the sublevel that is lowest in energy. As the atom moves into a region with a different light polarization, the light shifts of the sublevels are also different and the formerly most shifted sublevel moves up in energy. If the atom stays in the same sublevel, the energy difference is taken from the kinetic energy and the atom slows down. As soon as a different sublevel now has the lowest energy, optical pumping will preferentially take the atom to this level, from where it starts climbing the potential hill again. When the kinetic energy of the atoms becomes lower than the maximum light shift, atoms in a particular magnetic substate will be channeled in the spatially modulated potential. This is enhanced by the optical pumping to the deepest channel, which also causes the cooling effect. For positive detuning, optical pumping will drive the atom to the magnetic sublevel that is highest in energy. Consequently, channeling will be suppressed for positive detuning and enhanced for negative detuning in this polarization configuration. As coherences between the magnetic sublevels do not play an important role, the Sisyphus mechanism can easily be included in the semiclassical rate-equation-based Monte Carlo simulation of the experiment.

For the $\sigma^+\sigma^-$ cooling configuration, it is impossible to perform such a simple simulation. Coherences between the ground states cause the cooling effect. These cannot be included in this treatment, which only deals with the population of levels. For a description of this cooling mechanism, see Refs. [3–5].

B. Semiclassical treatment

In the semiclassical model we consider an ensemble of pointlike particles that is subject to a position and velocity dependent diffusion $D(x,v)$ and force $F(x,v)$. The evolution of the combined position and velocity distribution $W(x,v)$ is then governed by the Fokker-Planck equation. The average force and the diffusion coefficient are calculated using the operator description of sub-Doppler laser cooling by Nienhuis *et al.* [5].

The force and diffusion coefficients are given by

$$\mathbf{F}(\mathbf{r},\mathbf{v})=\langle\hat{\mathbf{f}}(t)\rangle, \tag{2}$$

$$2\overleftrightarrow{\mathbf{D}}(\mathbf{r},\mathbf{v})=\int d\tau\langle\hat{\mathbf{f}}(t)\hat{\mathbf{f}}(t+\tau)\rangle-\langle\hat{\mathbf{f}}(t)\rangle\langle\hat{\mathbf{f}}(t+\tau)\rangle+\text{c.c.}, \tag{3}$$

with $\hat{\mathbf{f}}$ the Heisenberg force operator with expectation value $\langle\hat{\mathbf{f}}\rangle=\mathrm{Tr}(\sigma\hat{\mathbf{f}})$. Here, the density matrix σ describes the internal states of the ensemble of atoms.

The radiation field is described by the classical electric field

$$\mathbf{E}(\mathbf{r},t)=\mathbf{E}_+(\mathbf{r})e^{-i\omega_L t}+\mathbf{E}_-(\mathbf{r})e^{i\omega_L t} \tag{4}$$

with ω_L the laser frequency. The field drives the transition between a lower level g and an upper level e, which may each be degenerate. In the rotating wave approximation, the atom-field coupling is governed by the Rabi operators $\hat{\mathcal{R}}=\boldsymbol{\mu}_{eg}\cdot\mathbf{E}_+\hat{b}/\hbar$ and $\hat{\mathcal{R}}^\dagger=\boldsymbol{\mu}_{ge}\cdot\mathbf{E}_-\hat{b}^\dagger/\hbar$ with $\boldsymbol{\mu}_{eg}=\boldsymbol{\mu}_{ge}^*$ the atomic dipole matrix and $\hat{b}$ and $\hat{b}^\dagger$ the atomic lowering and raising operators, respectively.

The force operator $\hat{\mathbf{f}}$ is determined by the commutator of the momentum operator with the Hamiltonian and is given by

$$\hat{\mathbf{f}}=\hbar[\nabla\hat{\mathcal{R}}+\nabla\hat{\mathcal{R}}^\dagger]. \tag{5}$$

In the low-velocity limit ($v\ll\Gamma/k$), the evolution equation of the density matrix is given by Nienhuis *et al.* [5]. We evaluate this numerically for a one-dimensional laser field, with a time dependent amplitude corresponding to the atomic motion along the atomic beam axis through the Gaussian laser beam profile. The force and diffusion coefficient working on an ensemble of atoms are now calculated as follows: We start out with a density matrix representing an ensemble of atoms located at position $\mathbf{r}$ and all polarized with a magnetic moment m in the direction of the laser beam. We follow the evolution of the density matrix, while at each time calculating the new position, momentum, and force. This results in ''classical particle trajectories'' for the center of mass of the atomic ensemble. The diffusion coefficient is calculated as the time autocorrelation of the force along the trajectory, as given in Eq. (3). Afterwards, the trajectory, which constitutes a δ-function momentum distribution, is broadened into a Gaussian momentum distribution using the calculated diffusion coefficient. This process is repeated for a number of different starting positions in the standing wave, for a number of initial velocities, and for all particular magnetic sublevels. Note that starting out with a density matrix containing an isotropic distribution over the magnetic substates gives a different result than starting the calculation with only a single magnetic substate and averaging this afterwards. The latter procedure more accurately reproduces

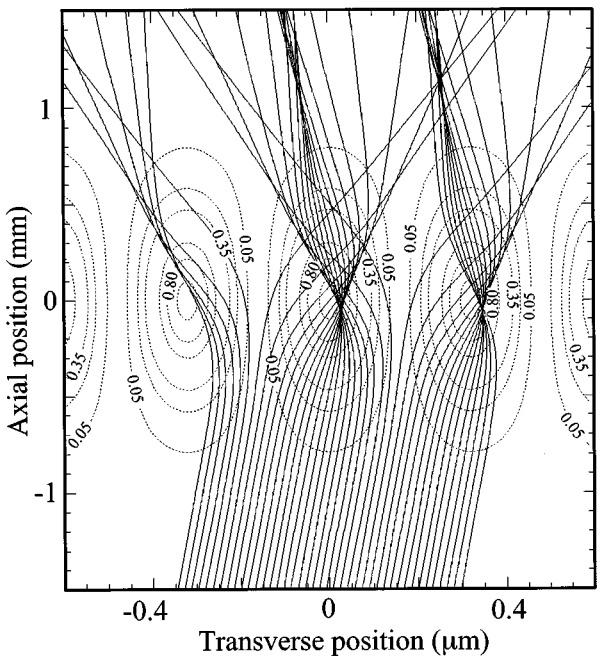

FIG. 1. ''Classical atom trajectories'' as calculated by the semiclassical treatment in a standing wave of linearly polarized light. Note that the exit velocity mostly depends on the incoming *position* in the standing wave. The dotted lines are contour lines of equal light shift. The labels on the contour lines display the fraction of the maximum light shift.

the actual final momentum distribution of the atomic ensemble, as the former procedure can only lead to a Gaussian distribution.

In Fig. 1 ''classical particle trajectories'' as calculated using the semiclassical model for atoms with an initial velocity of 0.1 ms^{-1} for 20 initial positions in a linearly polarized standing laser wave are shown. The light intensity as a function of the position is displayed as a contour plot in dashed lines. The particle trajectories are averaged over the different magnetic substates. Note that for different initial positions in the standing wave, we get dramatically different exit velocities. This is observed in the experiment as a strong broadening of the atomic beam. Note also that in this particular case there is a focal point almost in the middle of the standing wave: the dipole potentials induced by the laser field effectively act as a graded index lens for atoms with pitch 0.5. Consequently, a large fraction of the atoms has an final velocity $v_e = -v_i$.

C. Quantum Monte Carlo treatment

1. Basic theory

The quantum Monte Carlo treatment (QMC) is based on Mollow's treatment of resonant light scattering [23]. This treatment has been extended to a Monte Carlo simulation for a running laser wave by Blatt *et al.* [24]. Dum *et al.* [22] and Dalibard *et al.* [25] have further extended it to include arbitrary light field configurations and (magnetic) atomic substructure. We briefly summarize this treatment.

For an atom in a light field, the total Hamiltonian $\hat{H}$ is given by

$$\hat{H} = \frac{\hat{p}^2}{2M} + \hat{H}_{0A} + \hat{H}_{0F} + \hat{H}_{\mathrm{I}}(t), \tag{6}$$

where $\hat{p}$ is the momentum of the atom and M the mass. The operator $\hat{H}_{0A} = \omega_{eg}\hat{b}^{\dagger}\hat{b}$ is the Hamiltonian of the free atom, with $\hat{b} = |g\rangle\langle e|$ and $\hat{b}^{\dagger} = |e\rangle\langle g|$ the atomic lowering and raising operators, respectively. The kets $|e\rangle$ and $|g\rangle$ are the time-independent excited and ground states of the atom. The operator $\hat{H}_{0F}$ denotes the Hamiltonian of the free radiation field, and the interaction part $\hat{H}_{\mathrm{I}}$ is given by

$$\hat{H}_{\mathrm{I}}(t) = -\boldsymbol{\mu}_{eg}^{*} \cdot \hat{\mathbf{E}}^{\dagger}\hat{b} + \mathrm{H.c.} \tag{7}$$

Here, $\boldsymbol{\mu}_{eg}$ is the atomic dipole matrix and $\hat{\mathbf{E}}$ the electric field operator.

We assume that at time $t=0$, all radiation modes except the laser mode are empty. The wave function $\Psi(\mathbf{r},t)$ is split in partial wave functions $\Psi^n(\mathbf{r},t)$ with n spontaneously emitted photons. The zero-spontaneous emission partial wave function is written

$$\Psi^0(\mathbf{r},t) = C_g^0(\mathbf{r},t)|g,\{0\}\rangle + C_e^0(\mathbf{r},t)|e,\{0\}\rangle. \tag{8}$$

Equations of motion for the coefficients C_g^0 and C_e^0 only can be derived, with the spontaneous emission accounted for by a damping term. The modulus $|\Psi^0(t)|^2 = |C_g^0(t)|^2 + |C_e^0(t)|^2$ is equal to the probability that no spontaneous emission has occurred until time t. In a Monte Carlo implementation this probability is used to randomly determine the time at which the spontaneous emission takes place by taking a random number $\Upsilon \in [0,\ldots 1]$ and solving the equation

$$1 - |\Psi^0(t)|^2 = \Upsilon. \tag{9}$$

At this moment in the simulation, we assume no further interaction with the spontaneously emitted photon. The excited state part of the wave function is projected onto the ground state and renormalized. In the case of a two-level atom, this simply means starting over in the zero-photon ground state with $C_g(0) = 1$.

In case of a two-level atom in a running laser wave the complete time evolution of the coefficients C_g^0 and C_e^0 is given by Mollow [23]; it has been applied to a Monte Carlo simulation of cooling processes by Blatt *et al.* [24] and to resonance fluorescence photon statistics by us [26].

To include magnetic substructure, the wave function Ψ^0 can be expanded in time-independent states $|\alpha, m_\alpha\rangle$ with coefficients C_α and $\alpha = e$ or g. The superscript zero, denoting the fact that C_α only denotes that part of the wave function with no spontaneous emission yet, has been omitted. The operator $\hat{p}$, with eigenfunctions $|p\rangle$, is used to describe the atomic momentum in the direction of the laser. The motion perpendicular to the laser beam is treated classically. The product wave function is now represented by $|\alpha, m_\alpha, p\rangle$. If there is no spontaneous emission, the atomic momentum is quantized as $|p_0 + j\hbar k\rangle$ with p_0 the initial momentum and j an integer number. We now have a family $\mathcal{F}_{p_0}$ of states that are internally coupled only by stimulated processes. The states of this family are denoted by $|\alpha, m_\alpha, j\rangle$ and have coefficients $C^j_{\alpha m_\alpha}$. The momentum eigenvalues are $p_0 + j\hbar k$

with j even for the ground states and j odd for the excited states, respectively. An atom can leave the family of states by spontaneous emission to another family $\mathcal{F}_{p_0'}$.

The equations of motion governing the coherent evolution (the evolution until a spontaneous emission takes place) of the coefficients $C^j_{\alpha m_\alpha}(t)$ for a family with initial momentum $p_0=\hbar k_0$ are, in a one-dimensional laser configuration in the z direction, given by

$$i\hbar\frac{d}{dt}C^j_{gm_g}(t)=\left[\frac{\hbar^2}{2M}(jk+k_0)^2+\mu_B g_{j_g}B^z m_g\right]C^j_{gm_g}(t)+\frac{\mu_B g_{j_g}}{2}(B^x-iB^y)\sqrt{(j_g-m_g)(j_g+m_g+1)}\,C^j_{g(m_g+1)}(t)$$
$$+\frac{\mu_B g_{j_g}}{2}(B^x+iB^y)\sqrt{(j_g+m_g)(j_g-m_g+1)}\,C^j_{g(m_g-1)}(t)+\frac{\hbar\Omega^*_{eg}}{2}\langle j_g m_g 11|j_e(m_g-1)\rangle[\epsilon_1^{+*}C^{j+1}_{e(m_g-1)}(t)$$
$$+\epsilon_1^{-*}C^{j-1}_{e(m_g-1)}(t)]+\frac{\hbar\Omega^*_{eg}}{2}\langle j_g m_g 1-1|j_e(m_g+1)\rangle[\epsilon_{-1}^{+*}C^{j+1}_{e(m_g+1)}(t)+\epsilon_{-1}^{-*}C^{j-1}_{e(m_g+1)}(t)], \tag{10}$$

$$i\hbar\frac{d}{dt}C^j_{em_e}(t)=\left[\frac{\hbar^2}{2M}(jk+k_0)^2-\hbar(\Delta+i\Gamma/2)+\mu_B g_{j_e}B^z m_e\right]C^j_{em_e}(t)+\frac{\mu_B g_{j_e}}{2}(B^x-iB^y)\sqrt{(j_e-m_e)(j_e+m_e+1)}\,C^j_{e(m_e+1)}(t)$$
$$+\frac{\mu_B g_{j_e}}{2}(B^x+iB^y)\sqrt{(j_e+m_e)(j_e-m_e+1)}\,C^j_{e(m_e-1)}(t)+\frac{\hbar\Omega_{eg}}{2}\langle j_g(m_e+1)11|j_e m_e\rangle[\epsilon_1^{+}C^{j-1}_{g(m_e+1)}(t)$$
$$+\epsilon_1^{-}C^{j+1}_{g(m_e+1)}(t)]+\frac{\hbar\Omega_{eg}}{2}\langle j_g(m_e-1)1-1|j_e m_e\rangle[\epsilon_{-1}^{+}C^{j-1}_{g(m_e-1)}(t)+\epsilon_{-1}^{-}C^{j+1}_{g(m_e-1)}(t)]. \tag{11}$$

Here, the Rabi frequency is defined as for a two-level system by $\Omega_{eg}=[3\lambda_0^3 I/2\pi hc\tau]^{1/2}$ with I the light intensity of a single laser beam. $B^{\{x,y,z\}}$ denote the Cartesian components of the magnetic field. The relative strengths of the orthogonal circular polarization components $+1$ and -1 of the individual laser beams in the $+$ and $-$ directions are denoted by $\epsilon^{\pm}_{\pm 1}$.

2. Numerical implementation

For a simulation of our experiment, we choose a basis set of 30–40 momentum states to study the momentum evolution of the atomic wave. Since our experiment is done with metastable neon, we evaluate a $J=2\rightarrow J=3$ transition. With $12=5+7$ magnetic substates taken into account, we thus integrate 360 coupled differential equations using the well-known NAG routine D02BHF. The interaction time is divided into small time intervals, in which we assume a constant laser intensity. We start out with an atomic plane wave with momentum p_0, a random angular momentum m_g in the direction of the laser and in the ground state. This means that all coefficients $C=0$, except for $C^0_{gm_g}=1$. We integrate the equations of motion for the coefficients C until time $\tau_{\rm MC}$, at which Eq. (9) is fulfilled, with $|\Psi^0(t)|^2=\Sigma_j\Sigma_\alpha\Sigma_{m_\alpha}|C^j_{\alpha m_\alpha}|^2$. At this moment, we assume a photon to be spontaneously emitted. We make a random choice of the polarization of the emitted photon $q=-1$, 0, or 1 (with appropriate weighting factors, determined by the excited state wave function) and add a random recoil to the initial momentum k_0. Then, we collapse the wave function to the ground state as follows:

$$C^j_{gm_g}(0)\leftarrow\frac{\Sigma_{m_e}\langle j_g m_g 1q|j_e m_e\rangle C^j_{em_e}(\tau_{\rm MC})}{\sqrt{\Sigma_{m_g}|\Sigma_{m_e}\langle j_g m_g 1q|j_e m_e\rangle C^j_{em_e}(\tau_{\rm MC})|^2}}, \tag{12}$$

$$C^j_{em}(0)\leftarrow 0. \tag{13}$$

Then, a new random value Υ is chosen and the integration is restarted with the new values for the ground state coefficients. The resulting momentum distribution resulting from many shots is binned. For 1000 shots, the computing time is about two hours on an IBM RS6000/320 workstation.

As a result, we obtain the momentum distribution of the deflected beam profile. In Fig. 2 this distribution is shown for three different values of the initial momentum p_0, in the $\pi^x\pi^y$ laser configuration with a detuning $\Delta=-3.8\Gamma$, and an on-resonance saturation parameter for each of the counter-running laser beams at the center of the laser beam profile $s=I/I_0=6.2$, with the saturation intensity $I_0=\pi hc/3\lambda_0^3\tau$. In this situation, channeling of the atoms in the periodic potential induced by the light field should play an important role. For $p\approx 12\hbar k$ the kinetic energy of the atoms is equal to the maximum light shift. The sharp peaks in the figures represent the fraction of the atoms that has not spontaneously emitted a photon during the interaction. We observe that for initial momentum $p_0=0$, the atomic momentum distribution is redistributed over many momentum states by absorption-stimulated emission cycles. For $p_0=10\hbar k$, with a kinetic energy slightly smaller than the maximum light shift, the atoms are clearly pushed to $p=0$ by this process. For $p_0=14\hbar k$, the kinetic energy of the atoms is larger than the

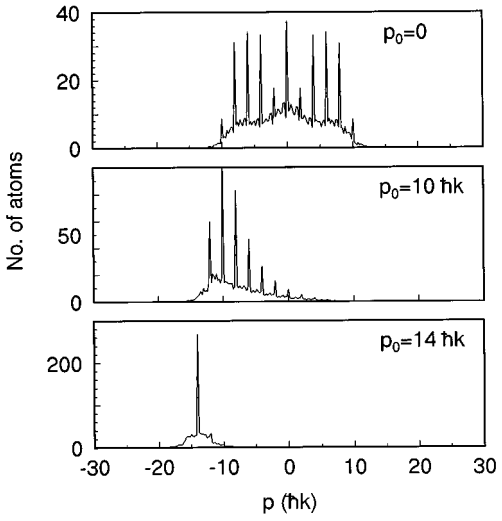

FIG. 2. Final momentum distributions from the QMC calculations for three different initial momenta. The laser configuration is $\pi^x\pi^y$, the detuning $\Delta=-3.8\Gamma$, and the saturation parameter $s=I/I_0=6.2$ for all initial momenta.

light shift and the stimulated redistribution process does not seem to occur. Only a single sharp peak at $p=p_0$ remains.

In Fig. 3 the resulting momentum distributions at lower intensity ($s\approx 4$) and smaller detuning ($\Delta=-2\Gamma$) are shown for the $\sigma^+\sigma^-$, $\pi^x\pi^y$, $\pi^x\pi^x$, and $\sigma^+\sigma^+$ laser configurations for $p_0=0$. In the latter two profiles, a strong stimulated redistribution is observed. For the former two profiles, a more Gaussian distribution is obtained with relatively few spikes, indicating that most atoms have spontaneously emitted a photon.

For the comparison of simulated momentum distributions with the experimental data in Sec. IV, the simulated profiles are then convolved with the experimental resolution. Of course all sharp peaks will then disappear.

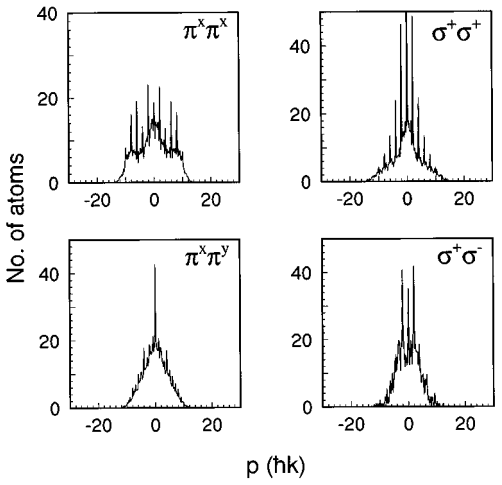

FIG. 3. Final momentum distributions from the QMC calculations for four different polarization configurations for initial momentum $p_0=0$. The detuning $\Delta=-2\,\Gamma$ for all graphs. The saturation parameter $s=4.1$ for the $\pi^x\pi^y$ and $\pi^x\pi^x$ configurations and $s=3.6$ for the $\sigma^+\sigma^-$ and $\sigma^+\sigma^+$ configurations.

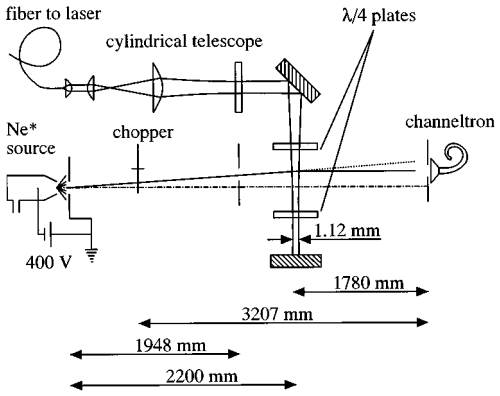

FIG. 4. An overview of the experimental setup. The atomic beam is collimated using two 50×500 μm slits. It is intercepted by a (quasi)standing laser field with a Gaussian waist radius of 0.56 mm on the backreflecting mirror. The deflected beam profile is analyzed using a channeltron electron multiplier with a 50×2000 μm entrance slit. The atomic beam is chopped to enable time-of-flight analysis of the atomic beam.

III. EXPERIMENT

A. Atomic beam setup

We use a supersonic beam of neon atoms, partly excited in a dc discharge to the metastable $^3P_2$ and $^3P_0$ states. The source creates a beam with an average velocity of $\approx 1200\ \mathrm{ms}^{-1}$, a velocity spread (FWHM) of $\approx 300\ \mathrm{ms}^{-1}$, and a center-line metastable beam intensity of $\approx 1.5\times 10^{13}\ \mathrm{s}^{-1}\ \mathrm{sr}^{-1}$.

The atomic beam is collimated to $<10^{-4}$ rad using two 50×500 μm slits located 5 mm and 1948 mm downstream from the source (Fig. 4). By moving the latter slit over 2 mm, the initial velocity in the direction of the laser beam $v_\perp$ can be changed in the range $-1\leqslant v_\perp(\ \mathrm{ms}^{-1})\leqslant +1$ with high selectivity. Over this range, the Doppler cooling force is very small. The interaction region is located 2200 mm downstream from the source.

The beam profile after deflection is analyzed using a movable channeltron electron multiplier with a 50×2000 μm entrance slit located 1780 mm downstream from the interaction region (Fig. 4). The channeltron detects metastable atoms as well as UV photons from the discharge source with a time resolution better than 100 ns.

The atomic beam is mechanically chopped to enable time-of-flight velocity analysis of the deflected atoms. The (FWHM) velocity resolution is given by $\Delta v/v=0.06$. The time-of-flight measurements greatly simplify the analysis of the deflected beam profiles, avoiding a convolution over both the interaction time and the axial velocity of the atoms.

The measuring time needed for the measurement of a deflection profile at a single initial transverse velocity is about 20 min. At typically 20 values of the initial velocity per full experimental curve, the total measurement time per curve is approximately 7 h.

B. Laser equipment

We used the transition from the neon metastable $\{(1s)^2(2s)^2(2p)^5(3s)\}^3P_2$ state, that has a lifetime of at least several seconds, [27] to the

$\{(1s)^2(2s)^2(2p)^5(3p)\}^3D_3$ state (lifetime $\tau=19.4$ ns), since this constitutes a pure closed-level system with only magnetic degeneracy. The natural linewidth of this transition is $\Gamma/2\pi=8.2$ MHz. The light, at 640.225 nm, is produced by a CW ring dye laser. Long-term drift is prevented by locking the laser frequency to a Zeeman-modulated and -shifted saturated absorption gas discharge cell.

In order to decouple the aligment of the laser from the alignment of the experiment, the laser beam is transported to the saturated absorption setup and to the actual experiment via single mode, polarization preserving fiber.

The laser beam has a Gaussian waist on the backreflecting mirror (see Fig. 4) with a radius of 0.56 mm ($1/e^2$ intensity drop) in the atomic beam direction, and 2.5 mm in the other dimension. The wavefront curvature is less than 25 μrad over the interaction region. The 0.5 mm high atomic beam is homogeneously illuminated to within 2%, and the intensity imbalance between the laser beams is smaller than 2% as well.

The laser beam is aligned perpendicular to the collimated atomic beam by tuning the laser resonant to the pumping transition to the $\{(1s)^2(2s)^2(2p)^5(3p)\}\alpha_8$ state (Paschen numbering), that can cascade to the ground state. The angle between laser and atomic beam is then varied to optimize the pumping efficiency, as monitored by the metastable signal loss. This ensures the laser beam will be perpendicular to the atomic beam to within 1 mrad.

The magnetic field in the interaction region is controlled by a full set of Helmholtz coils. The magnetic field was zeroed by using the Hanle effect on the pumping transition to the $\{\alpha_8\}$ state. Since this is a $J_e=J_g$ transition, the transition from $m_g=0$ to $m_e=0$ is forbidden. Consequently, when the laser is linearly polarized, inducing $\Delta m=0$ transitions, the atoms in the $m_g=0$ ground state will not be depleted. This results in a decrease in the pumping efficiency. However, if there is a small magnetic field, the magnetic sublevels will be mixed up by Larmor precession, and eventually the atoms initially in the $m=0$ sublevel will also be depleted, increasing the pumping efficiency and thus decreasing the metastable atom signal. This allowed us to reduce the magnetic field to $B<5$ mG in the interaction region.

C. Data analysis

To measure a deflected beam profile, a time-of-flight spectrum is taken at each detector position. The measured counts in one particular time-of-flight channel at different detector positions form a beam profile for a monoenergetic atomic beam. Such a profile for 1200 ms^{-1} atoms in the $\pi^x\pi^y$ polarization configuration is shown in Fig. 5. The signal with ''laser on'' is denoted by circles, the signal with ''laser off'' by squares. The undeflected peak in the laser on profile is from ^{20}Ne atoms in the $^3P_0$ metastable state and ^{22}Ne atoms in both metastable states, which are not deflected. Together, these represent 25.0% of the total signal, which is consistent with the natural abundance of the neon isotopes and the statistical ratio of 5:1 between the $^3P_2$ and $^3P_0$ metastable state populations. This ratio has proven to be very stable. The deflected beam profile is obtained by substracting 25.0% of the laser off signal from the laser on signal. The initial velocity is $v_\perp=0.10$ ms^{-1} in this figure. We

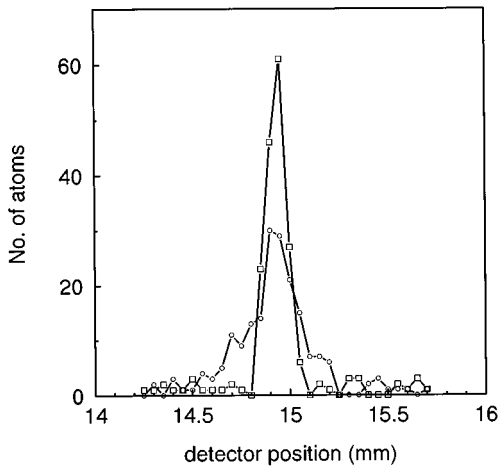

FIG. 5. A typical deflected beam profile for the $\pi^x\pi^y$ polarization configuration. In squares, the initial beam profile is shown, and in circles the deflected beam profile is shown, both for the 1200 ms^{-1} time-of-flight channel. The initial velocity in the direction of the laser is 0.1 ms^{-1} in this figure. The laser detuning in this figure is -2Γ, and the saturation parameter $s=4.0$.

can observe both a broadening and a deflection of the atomic beam. Using the time-of-flight analysis this can unambiguously be related to a velocity change Δv and the spread σ_v therein.

In order to reduce the statistical errors due to the low count rate, all time-of-flight channels are processed simultaneously in the following manner. First, for each time-of-flight channel the axial velocity of the detected atoms is calculated and the transverse velocity transfer profile (i.e., $\Delta v_\perp$ as a function of $v_\perp$) is determined from the axial velocity, collimating slit position and detected beam profile. Next, to account for the different interaction times, the velocity transfer profiles are transformed to acceleration profiles by dividing by the effective interaction time:

$$a_\perp=\frac{\Delta v_\perp(v_{\mathrm{ax}})}{\tau_{\mathrm{eff}}(v_{\mathrm{ax}})}=\frac{\Delta v_\perp(v_{\mathrm{ax}})v_{\mathrm{ax}}}{l_{\mathrm{eff}}}. \tag{14}$$

The effective interaction time $\tau_{\mathrm{eff}}(v_{\mathrm{ax}})$ is defined as the time an atom with axial velocity v_{ax} needs to traverse a laser beam with an ''equivalent square profile.'' This is defined as the square profile with the same integrated area and variance as the Gaussian laser beam profile, i.e., a profile with width $l_{\mathrm{eff}}=\sigma\sqrt{12}$ and height $I_{\mathrm{eff}}=\sqrt{\pi/6}I_0$ for a Gaussian with variance σ^2 and maximum height I_0. The array of acceleration profiles obtained in this way is fitted simultaneously to the sum of two Gaussians for the shape and to the supersonic axial velocity distribution for the normalization of each time-of-flight channel using a least-squares procedure. The two-Gaussian fit function was found to yield a satisfactory fit to the experimental data in all cases and hence yields reliable values for the deflection and the broadening of the atomic beam. Determination of the rms broadening directly from the atomic beam profile instead of from the Gaussian fit is possible as well, but poses serious numerical problems due to the noise in the wings of the deflection pattern. With the

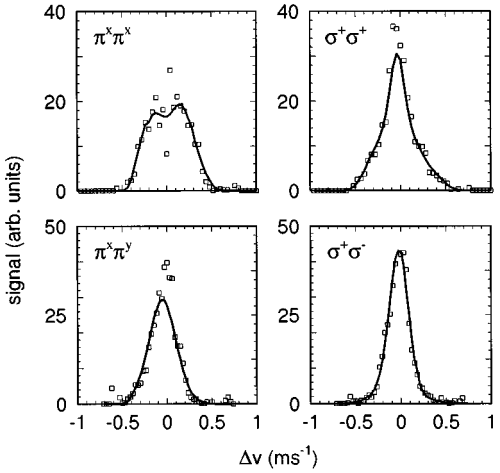

FIG. 6. Deflected beam profiles averaged over the time-of-flight spectrum for the $\pi^x\pi^x$, $\sigma^+\sigma^+$, $\pi^x\pi^y$, and $\sigma^+\sigma^-$ polarization configurations. Here, the horizontal axis is velocity change. The two-Gaussian fit curve is represented by the full line.

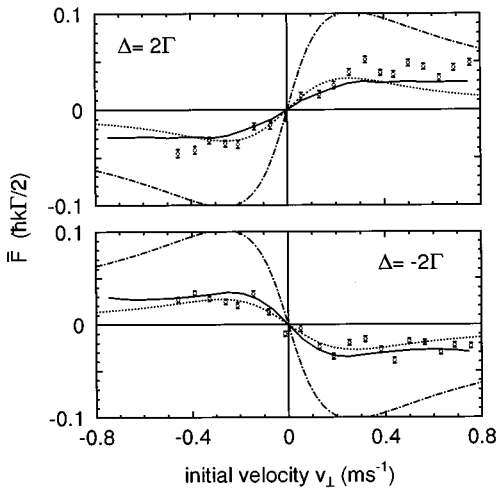

FIG. 7. The force as a function of the initial velocity $v_\perp$ for the $\sigma^+\sigma^-$ configuration. The laser detuning is $\Delta = 2\,\Gamma$ for the upper graph and $\Delta = -2\,\Gamma$ for the lower graph. The saturation parameter for both curves is $s = 3.6$. The dash-dotted line indicates the steady-state drag force for these parameters. The results of the QMC and SC calculations are represented by the full and dotted lines, respectively. The error bars in this figure, as well is in following figures, represent 1σ statistical error intervals resulting from the errors in the parameters of the fitted deflected beam profiles.

procedure described above, the statistical errors are greatly reduced while only introducing a spread in $v_\perp$ discussed in Sec. III A.

In Fig. 6 velocity transfer profiles and two-Gaussian fits thereof are displayed for an initial velocity $v_\perp = 0$ and four different polarization configurations. In the $\sigma^+\sigma^-$ polarization configuration, an almost Gaussian broadening of the atomic beam caused by momentum diffusion is observed. For the $\pi^x\pi^x$ and the $\sigma^+\sigma^+$ configuration, effects of channeling in the standing wave are clearly visible through the broad base of the deflection curve. For the $\pi^x\pi^y$ configuration this is less clear. The effects of channeling will be discussed in detail in Sec. IV B.

IV. RESULTS AND DISCUSSION

In the following subsections we present detailed experimental results for the four polarization configurations mentioned in the preceding section. Graphs of the force and diffusion coefficient vs the transverse velocity are presented for the $\sigma^+\sigma^-$ configuration, curves of the average transverse velocity change and induced velocity spread for the other configurations. Measured beam profiles are presented as well for the channeling (standing wave) configurations. In all graphs, calculated curves are shown as well.

A. The $\sigma^+\sigma^-$ polarization configuration

In this polarization configuration the force on the atom does not depend on the initial position of the atom in the quasistanding wave. Therefore fit parameters can directly be related to an average force and a diffusion coefficient. In Fig. 7 the force in the $\sigma^+\sigma^-$ polarization configuration for laser detunings of equal magnitude but reversed sign are plotted as a function of the initial velocity. Also, the results from the quantum Monte Carlo (QMC) simulations, indicated by the full lines, and the semiclassical (SC) calculations, indicated by the dotted lines, as discussed in Secs. II C and II B, respectively, are shown. The force is scaled to the maximum radiation pressure force $\hbar k\Gamma/2 = 2.7\times10^{-20}$ N. Clearly visible is the dispersion like shape of the force. Although considerably larger than the Doppler force, the force is still much smaller than the steady-state drag force, as indicated by the dash-dotted line. This is caused by a transient effect: following the argument in Sec. II A, the Larmor frequency induced by the topological magnetic field is smaller than the reciprocal of the interaction time. Notwithstanding, this represents the first direct measurement of a sub-Doppler cooling force on neutral atoms. We observe that the force reverses as expected when the sign of the detuning is changed. The small difference between the SC and the QMC model is mainly caused by the fact that the SC calculations do not include the Doppler force.

In Fig. 8 the diffusion coefficients are plotted as a function of the initial velocity for these measurements. The diffusion coefficient is scaled by $\hbar^2k^2\Gamma/4 = 1.4\times10^{-47}$ kg^2 m^{-2} s^{-3}. Again, both theoretical calculations are displayed as well, showing good agreement. Note the differences between the results of the SC and QMC calculations near $v_\perp = 0$. The decrease in diffusion coefficient predicted by the SC model does not show up in either the experiments or the QMC calculations. We therefore consider this an artifact of the semiclassical calculation. It originates from considering the whole ensemble of atoms to follow a single ''averaged trajectory.'' The diffusion is calculated as the time autocorrelation of the force along this trajectory. When the force strongly depends on the velocity, this procedure is incorrect. The base level of the diffusion at large $v_\perp$ is well reproduced. The differences between the experimental and theoretical curves in the positive detuning curves are probably caused by a systematic error in the experimental determination of the laser detuning as discussed in Sec. III. The agreement can be largely improved by adjusting the detuning in the theoretical calculations by less than 0.5Γ. However,

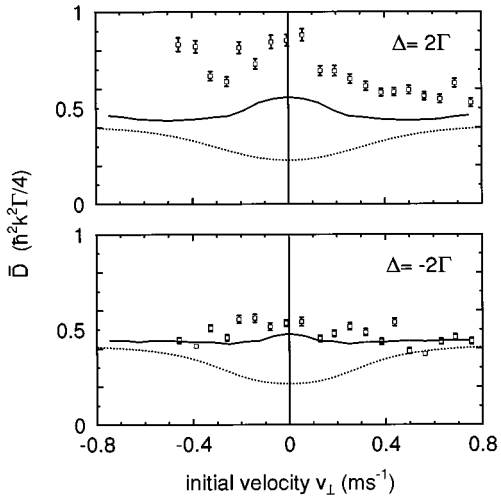

FIG. 8. The diffusion constant as a function of the initial velocity $v_\perp$ for the situation of Fig. 7. QMC and SC calculations are represented by the full and dotted lines, respectively.

for clarity the experimentally determined values are used as input for the calculations. In contrast to the SC calculations, the QMC calculations predict a small increase in the diffusion coefficient around $v_\perp = 0$. This increase is too small to be visible in the experiment. So far, we have found no physical interpretation of this effect.

In Fig. 9 the force as a function of the initial velocity is shown for three different laser intensities at the same laser detuning, as well as the results from both the QMC simulations and the SC calculations. The agreement of both models with the experiment is excellent. Again the differences between the models are caused by the omission of the Doppler

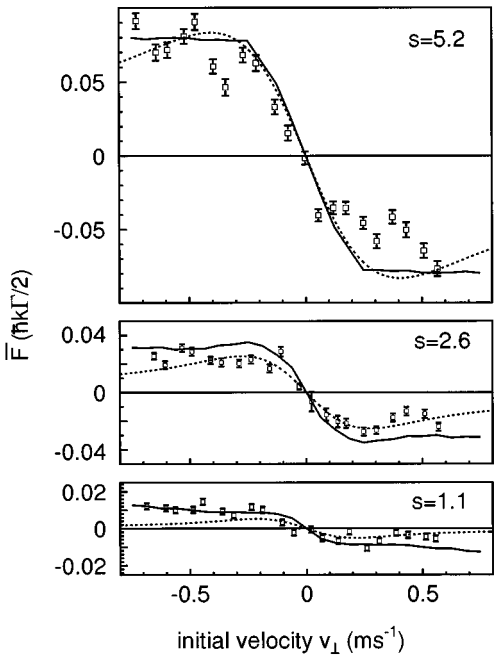

FIG. 9. The force as a function of initial velocity $v_\perp$ for three laser intensities in the $\sigma^+\sigma^-$ configuration. Also the SC (dotted line) and QMC (full line) calculations are shown. In all curves the detuning $\Delta = -1.6\Gamma$.

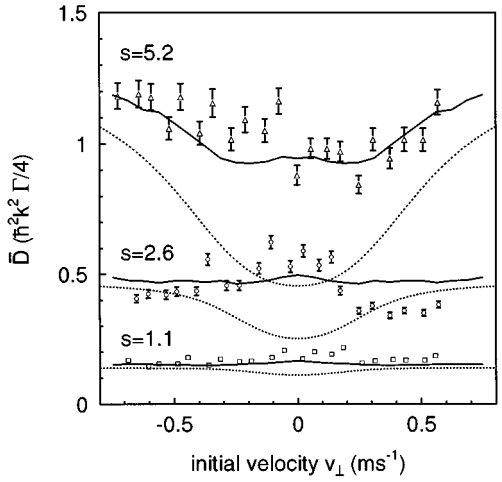

FIG. 10. The diffusion constant as a function of initial velocity $v_\perp$ for the situation of Fig. 9.

force in the SC model. Note that the calculations are carried out without any free parameters. The calculated curves show that the maximum sub-Doppler cooling force increases quadratically with the laser intensity. This can be understood by the following argument: the steady state cooling force increases linearly and the transient effect is reduced with increasing laser intensity.

For the diffusion coefficient, as displayed in Fig. 10, again a large difference between the SC model and both the experimental data and the QMC curves is observed due to the effect discussed earlier. The agreement of the QMC calculations with the measurements is excellent, whereas the large decrease in the diffusion coefficient near $v_\perp = 0$ in the SC calculations for high laser intensity is not reproduced by either the QMC calculations or the experimental data.

The oscillation visible in all plots of the experimental force as a function of the initial velocity is not reproduced by either theoretical model. In the experiment, however, it is reproducible and has a period of approximately 0.2 ms^{-1}. So far, these oscillations have not been explained. For the moment, we attribute it to an experimental artifact.

B. Channeling in a standing wave

In a purely standing wave of either linearly or circularly polarized light, the atoms can be deflected by the periodic potential formed by the differing light shift in the nodes and the antinodes of the field. In this configuration, there should be only the Doppler cooling force present due to the lack of polarization gradients. In Fig. 11 deflected beam profiles in standing waves are shown for an initial velocity $v_\perp = 0$ ms^{-1}, 0.17 ms^{-1}, and 0.40 ms^{-1}. The results from the QMC calculations are plotted as well. We now introduce the capture velocity v_c, which is defined as the velocity for which kinetic energy of the atoms is equal to the height of a potential hill. For the situation of Fig. 11, $v_c = 0.21$ ms^{-1} for the linear polarization data and $v_c = 0.26$ ms^{-1} for the circular polarization data.

For $v_\perp = 0$ (bottom frame), symmetric but strongly broadened profiles are observed. At $v_\perp \approx v_c$ (middle frame), a structure with two maxima is observed for both polarizations. If $v_\perp > v_c$ (top frame) the atomic beam will only be

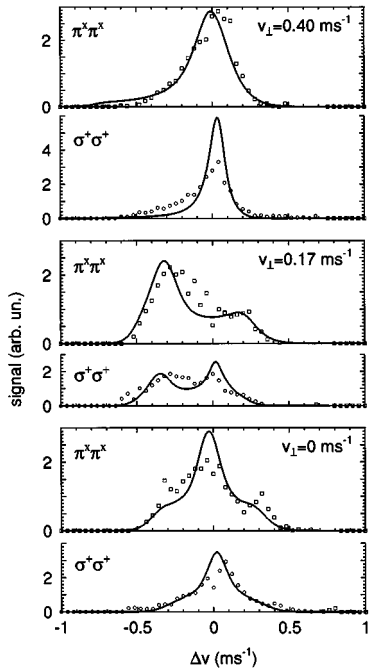

FIG. 11. Deflected beam profiles for the initial velocity $v_\perp > v_c$ (upper frame), $v_\perp < v_c$ (middle frame), and for $v_\perp = 0$ (lower frame) in the $\pi^x\pi^x$ and $\sigma^+\sigma^+$ polarization configurations (pure standing waves with linear and circular polarization). The data points for linear and circular polarization are denoted by squares and circles, respectively. The laser detuning $\Delta = -2.0\Gamma$ for all graphs. The saturation parameter $s = 4.1$ for linear polarization and 3.5 for circular polarization, resulting in $v_c = 0.21$ ms^{-1} and $v_c = 0.26$ ms^{-1}, respectively. The full line represents the results of the QMC calculations.

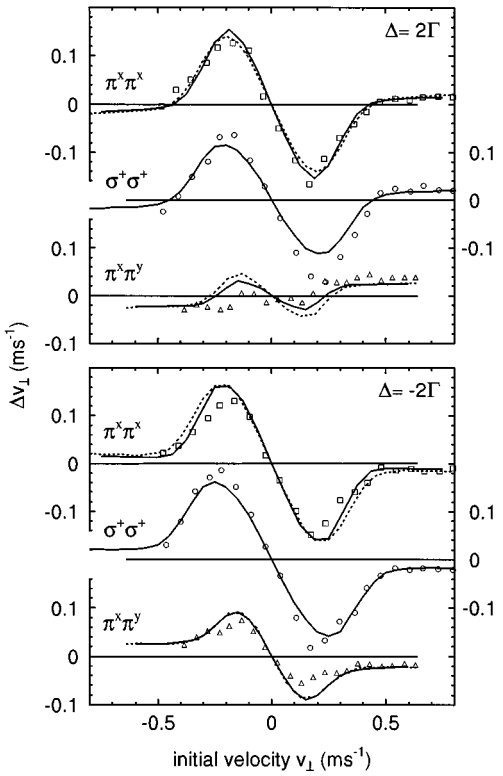

FIG. 12. The average velocity change Δv as a function of initial velocity $v_\perp$ in a linearly polarized standing wave (squares, top data in each frame), in a circularly polarized standing wave (circles, middle data), and in the $\pi^x\pi^y$ configuration (triangles, bottom data), for equal but reversed detunings. The detuning $\Delta = \pm 2\,\Gamma$ and the saturation parameter $s = 4.2$ for the $\pi^x\pi^x$ data, $s = 3.5$ for the $\sigma^+\sigma^+$ data, and $s = 4.0$ for the $\pi^x\pi^y$ data. The results from the QMC and RE calculations are represented by the full and dotted lines, respectively (RE results are only presented for $\pi^x\pi^x$ and $\pi^x\pi^y$).

deflected by the Doppler force and is just broadened by spontaneous emission. This threshold behavior is also apparent when we calculate the broadening and the average final velocity from the deflected beam profiles. When the initial velocity is below v_c, the atomic beam is strongly broadened and the average final velocity is almost zero. For initial velocities above v_c, the broadening is less and the final velocity is close to the initial velocity.

In Fig. 12 the average velocity change Δv as a function of $v_\perp$ for equal magnitude but reversed laser detunings Δ at the same laser intensity is shown for a linearly polarized standing wave (top curves in both frames), for a circularly polarized standing wave (middle curves), and for orthogonal linear polarization of the laser beams ($\pi^x\pi^y$). The latter configuration will be discussed in the next section. For a standing wave, we clearly see that the velocity change does not depend on the detuning. Just the small offsets in the tails of the profiles indicate residual effects of Doppler cooling. The agreement with the QMC simulations, indicated by the full lines, is excellent. The agreement with the results from the simple rate-equation-based model (RE) as indicated by the dashed lines (not shown for circular polarization) is excellent as well. Consequently the physical picture of channeling is correct to a high degree.

It should be stressed that, although the average velocity is reduced to zero in this configuration, it is *not* a cooling process. The final velocity of the atoms just depends more strongly on the position at which they enter the standing wave than on the initial velocity. This can be experimentally observed as a strongly enhanced broadening of the atomic beam, as shown in Fig. 13. In this figure we plot σ_v as a function of $v_\perp$ for the measurements in Fig. 12. The strong broadening for small $v_\perp$ does not depend on the laser detuning, as would be the case for a cooling process. With an even better resolution of the final velocity, diffraction effects could be observed in the deflected beam profiles.

For circular polarization, the experimental data and the QMC calculations do not agree as well as for linear polarization, athough the agreement is still quite satisfactory. The differences are probably due to an error in the experimental values of the laser detuning as discussed in Sec. III B. At zero initial velocity, we observe in the deflected beam profile (Fig. 11, bottom curve) a rather sharp peak at $\Delta v = 0$ and a broader underlying structure. For $v_\perp < v_c$ the underlying structure has shifted and has a long tail under the undeflected peak. For $v_\perp > v_c$, we only observe one peak, which is only slightly broadened by spontaneous emission. In this situation, the experimental velocity transfer profile is broader than the theoretically calculated profile. The small peak at $\Delta v = 0$ in the first two situations is caused by the atoms that are initially in the $m = -2$ sublevel. Due to the small Clebsch-Gordan coefficient for excitation by σ^+-polarized

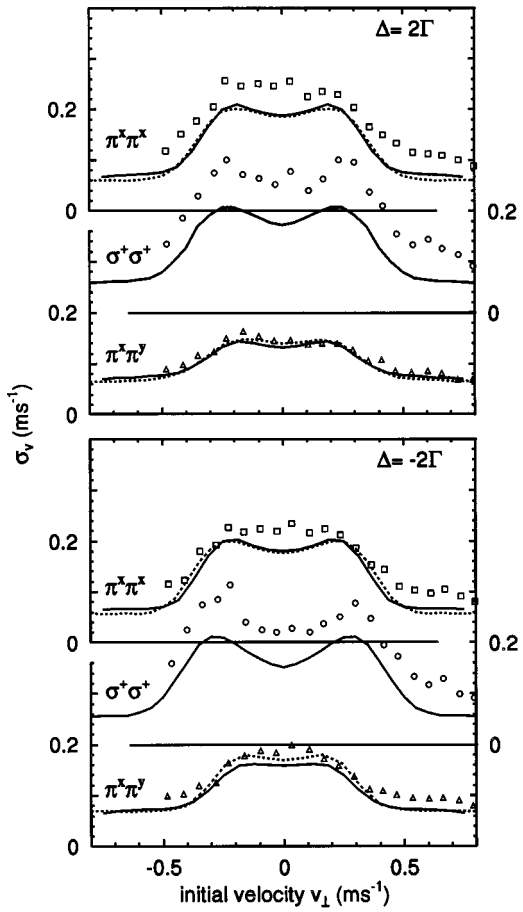

FIG. 13. The spread in final velocity σ_v as a function of initial velocity $v_\perp$ for the situation of Fig. 12.

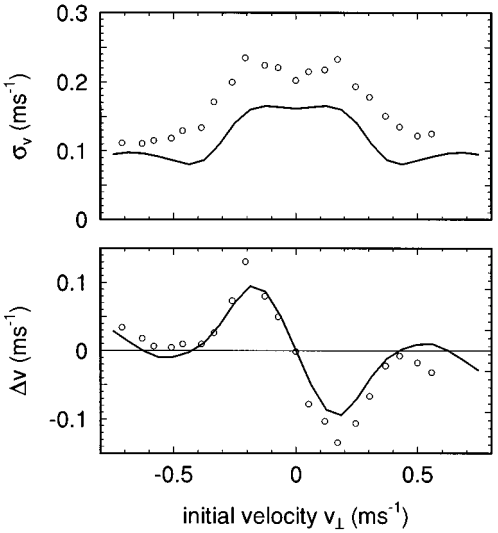

FIG. 14. The average velocity change Δv (lower part) and the final velocity spread σ_v (upper part) for a circularly polarized standing wave with a magnetic field perpendicular to the direction of the laser beam. The detuning $\Delta = -1.6\Gamma$, the saturation parameter $s = 2.6$, and the magnetic field $B = 0.753$ G for these curves. The results from the QMC simulations are represented by the full line, showing good agreement.

light to the $m = -1$ upper state sublevel, these atoms have an appreciable probability of not being excited at all by the laser beams. Hence these atoms will hardly be deflected. This effect is not present for linear polarization.

If with a circularly polarized standing wave a magnetic field is applied perpendicular to the propagation direction of the laser light, the well-known magnetically induced laser cooling (MILC) force [4,8–10] should be visible. The effects of this force are, however, largely obscured by the deflection caused by channeling. For a higher magnetic field, velocity selective magnetic resonance laser cooling (VSMRLC) [10–12] should be visible. In Fig. 14 the velocity change and broadening in pure standing wave of σ polarized light in a magnetic field perpendicular to the laser field $B = 0.753$ G are shown. Near zero initial velocity the channeling effect is dominant, but at higher initial velocity some extra features are observed. The resonant velocity for VSMRLC is 0.50 ms^{-1}. The QMC simulation again excellently reproduces the results from the experiments.

C. The $\pi^x\pi^y$ polarization configuration

In the $\pi^x\pi^y$ configuration (usually called lin$\perp$ lin) the atoms can, depending on their initial magnetic substate, be channeled in the potential wells formed by the polarization gradient. Again we expect a largely different behavior for atoms entering the laser field at different positions or in a different magnetic substate. Consequently, the broadening of the atomic beam is also expected to be non-Gaussian. In this case, there is a large difference between positive and negative detuning caused by the actual cooling process. The atoms are always optically pumped to the most light-shifted substate. For positive detuning this means that the atoms are always pumped to the highest potential hill, which is not a stable situation. For negative detuning, the reverse is true and the atoms will accumulate in potential valleys.

In Fig. 12 the average velocity change Δv of the atomic beam in this configuration for positive and negative detuning is shown in the bottom part of both frames (triangular data points). Notice that the average effects of cooling and channeling almost cancel for positive detuning, whereas for negative detuning the effects add up. In both frames, also the results from the QMC (full line) and RE (dashed line) calculations are displayed. The excellent agreement between the QMC and RE simulations indicate that the physical picture associated with the $\pi^x\pi^y$ cooling mechanism is correct to a high degree. In Fig. 13 the spread in final velocity σ_v is displayed for these situations. In these curves the difference between positive (upper part) and negative (lower part) detuning is clearly visible. In the latter case the channeling effect is enhanced by the optical pumping to the magnetic substate that is lowest in energy. This enhanced channeling effect causes a stronger broadening for $v_\perp$ smaller than the threshold. In the former case, the channeling is decreased by the optical pumping. Note the excellent agreement of the experimental data with the results from both the QMC simulation (full line) and RE simulation (dashed line).

In Fig. 15 the velocity change Δv is given for three different intensities at the same laser detuning. We can observe that both the maximum velocity change due to the channeling mechanism and the capture velocity v_c of this mechanism increase with increasing intensity as expected. The re-

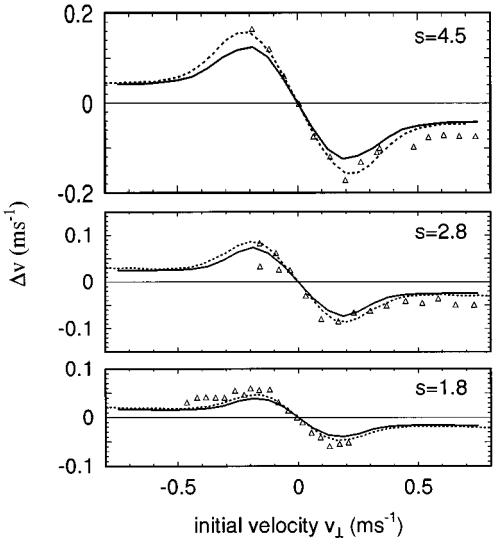

FIG. 15. The average velocity change Δv as a function of initial velocity $v_\perp$ in the $\pi^x\pi^y$ polarization configuration for three different values of the laser intensities $s=I/I_0$. The detuning $\Delta=-1.6\Gamma$ for all profiles. The results from the QMC and RE simulations are represented by the full and dashed lines, respectively.

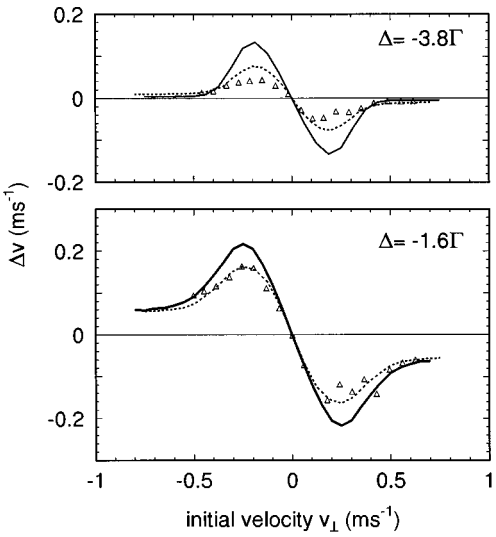

FIG. 17. The average velocity change Δv as a function of initial velocity $v_\perp$ in the $\pi^x\pi^y$ polarization configuration for two different values of the laser detuning Δ. The saturation parameter $s=I/I_0=6.1$ for both profiles. The results from the QMC and RE simulations are represented by the full and dashed lines, respectively.

sults from the QMC and RE simulations are shown, indicated by the full and dashed lines, respectively. The agreement of the experimental data and both simulations is good. The final velocity spread σ_v for these situations is shown in Fig. 16. Herein the increase in capture range can be observed as well: for initial velocities larger than the capture range the beam is only broadened by spontaneous emission, while for smaller initial velocity the final velocity depends on the initial position of the atom in the spatially modulated potential. Note that for $s=4.5$, the spread in deflection near $v_\perp=0$ is smaller than for larger $v_\perp$.

In Fig. 17 the velocity change Δv is shown for two different detunings at the same laser intensity, as well as the result from both the QMC and RE simulations. The channeling effect decreases with increasing detuning as expected. In the final velocity spread, as displayed in Fig. 18, we observe a large difference between these situations. For large detuning (upper part), the broadening due to channeling is dominant and causes the broadening to be large. For smaller detuning (lower part) the optical pumping rate is much larger and the Sisyphus mechanism is relatively important. This is visible as a large decrease in broadening for small $v_\perp$. The agreement of both simulations with the experimental data is good for both situations.

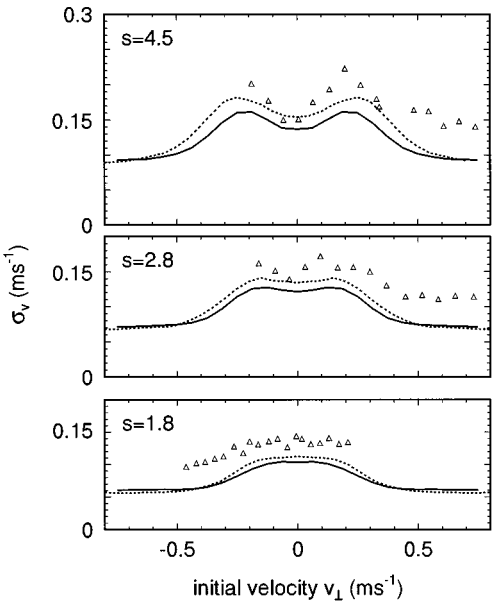

FIG. 16. The velocity spread σ_v as a function of initial velocity $v_\perp$ for the situation of Fig. 15.

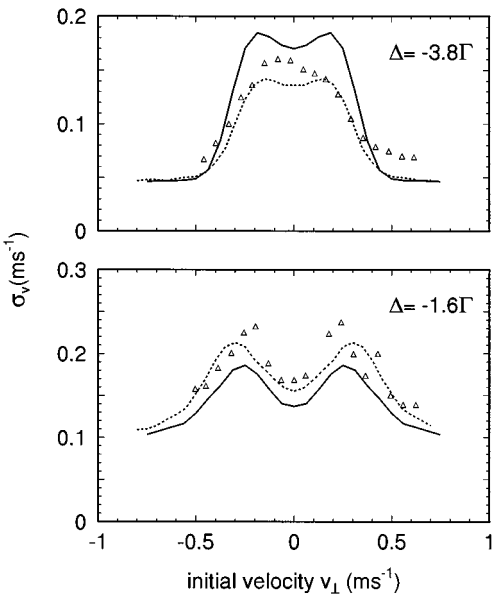

FIG. 18. The velocity spread σ_v as a function of initial velocity $v_\perp$ for the situation of Fig. 17.

V. CONCLUSIONS

We have presented direct measurements of the velocity dependence of $\sigma^+\sigma^-$ sub-Doppler laser cooling forces and diffusion constants for neon atoms. We compared the experimental results to a simulation based on a quantum Monte Carlo approach as well as a semiclassical density matrix calculation. We demonstrate excellent quantitative agreement with the experimental data without any free parameters.

The effects of channeling in the periodic potential induced by a standing laser wave of either circular or linear polarization have been demonstrated. These results show excellent agreement with simulations based on a simple rate-equation approach, as well as with the more rigorous quantum Monte Carlo calculations.

Experimental results obtained for the $\pi^x\pi^y$ cooling configuration are very well reproduced by the rate-equation-based calculations as well. This demonstrates that the simple physical ''Sisyphus'' picture for the cooling mechanism is valid to a high degree.

The dynamics of the cooling process for both $\sigma^+\sigma^-$ and $\pi^x\pi^y$ configurations have been studied in great detail as a function of laser detuning and intensity. The experimental data and theoretical calculations provide a good insight in the dynamics of the cooling process.

For future extensions, we intend to investigate the transition to the steady state by varying the interaction time and keeping the laser intensity constant during the interaction. As we go from a single oscillation in a potential well to a large number, quantization of the atomic motion will become visible. In fact, we will be able to excite selectively one particular vibrational state in the potential well. Replacing the two counterpropagating laser beams in the interaction region with the field in a small, very high finesse optical cavity gets us in the regime where not only the atomic motion but also the exciting field has to be quantized. Other extensions include sub-Doppler cooling forces and dark states in two-dimensional laser fields.

ACKNOWLEDGMENTS

This work is financially supported by the Dutch Foundation for Fundamental Research on Matter (FOM) (M.D.H.), the Royal Dutch Academy of Sciences (KNAW) (v.d.S., E.J.D.V.), the North Atlantic Treaty Organization (NATO) (M.D.H., K.A.H.V.L., E.J.D.V., and H.J.M.), the National Science Foundation (NSF) (E.J.D.V., H.J.M.), and the Office of Naval Research (ONR) (E.J.D.V., H.J.M.).

[1] P.D. Lett, R.N. Watts, C.I. Westbrook, W.D. Phillips, P.L. Gould, and H.J. Metcalf, Phys. Rev. Lett. **61**, 169 (1988).
[2] Y. Shevy, D.S. Weiss, P.J. Ungar, and S. Chu, Phys. Rev. Lett. **62**, 1118 (1989).
[3] J. Dalibard and C. Cohen-Tannoudji, J. Opt. Soc. Am. B **6**, 2023 (1989).
[4] P.J. Ungar, D.S. Weiss, S. Chu, and E. Riis, J. Opt. Soc. Am. B **6**, 2058 (1989).
[5] G. Nienhuis, P. van der Straten, and S.-Q. Shang, Phys. Rev. A **44**, 462 (1991).
[6] D.S. Weiss, E. Riis, Y. Shevy, P.J. Ungar, and S. Chu, J. Opt. Soc. Am. B **6**, 2072 (1989).
[7] B. Sheehy, S.-Q. Shang, P. van der Straten, and H. Metcalf, Chem. Phys. **145**, 317 (1990).
[8] B. Sheehy, S.-Q. Shang, P. van der Straten, S. Hatamian, and H. Metcalf, Phys. Rev. Lett. **64**, 858 (1990).
[9] O. Emile, R. Kaiser, C. Gerz, H. Wallis, A. Aspect, and C. Cohen-Tannoudji, J. Phys. II France **3**, 1709 (1993).
[10] M.D. Hoogerland, H.C.W. Beijerinck, K.A.H. van Leeuwen, P. van der Straten, and H.J. Metcalf, Europhys. Lett. **19**, 669 (1992).
[11] S.-Q. Shang, B. Sheehy, P. van der Straten, and H. Metcalf, Phys. Rev. Lett. **65**, 317 (1990).
[12] S.-Q. Shang, B. Sheehy, H. Metcalf, P. van der Straten, and G. Nienhuis, Phys. Rev. Lett. **67**, 1094 (1991).
[13] P. van der Straten, S.-Q. Shang, B. Sheehy, H. Metcalf, and G. Nienhuis, Phys. Rev. A **47**, 4160 (1993).
[14] J.S. Padua, C. Xie, R. Gupta, H. Batelaan, T. Bergeman, and H. Metcalf, Phys. Rev. Lett. **70**, 3217 (1993).
[15] R. Grimm, J. Söding, Yu. B. Ovchinnikov, and A.I. Sidorov, Opt. Commun. **98**, 554 (1993).
[16] R. Gupta, C. Xie, S. Padua, H. Batelaan, and H. Metcalf, Phys. Rev. Lett. **71**, 3087 (1993).
[17] H. Metcalf and P. van der Straten, Phys. Rep. **244**, 203 (1995).
[18] V.S. Letokhov, M.A. Ol'shaniĭ, and Yu.B. Ovchinnikov, Quantum Semiclass. Opt. **7**, 5 (1995).
[19] M.D. Hoogerland, H.F.P. de Bie, H.C.W. Beijerinck, K.A.H. van Leeuwen, P. van der Straten, E.J.D. Vredenbregt, and H.J. Metcalf, Phys. Rev. Lett. **72**, 3332 (1994).
[20] M.G. Prentiss and S. Ezekiel, Phys. Rev. Lett. **56**, 46 (1986).
[21] C. Salomon, J. Dalibard, A. Aspect, H. Metcalf, and C. Cohen-Tannoudji, Phys. Rev. Lett. **59**, 1659 (1987).
[22] R. Dum, P. Zoller, and H. Ritsch, Phys. Rev. A **45**, 4879 (1992).
[23] B. Mollow, Phys. Rev. A **12**, 1919 (1975).
[24] R. Blatt, W. Ertmer, P. Zoller, and J.L. Hal, Phys. Rev. A **34**, 3022 (1986).
[25] J. Dalibard, Y. Castin, and K. Mølmer, Phys. Rev. Lett. **68**, 580 (1992).
[26] M.D. Hoogerland *et al.*, Phys. Rev. Lett. **65**, 1559 (1990).
[27] N. Small-Warren and L. Chin, Phys. Rev. A **11**, 1777 (1975).